nature climate change

ARTICLES

https://doi.org/10.1038/s41558-021-01074-x

Check for updates

Climate change decisive for Asia's snow meltwater supply

Philip D. A. Kraaijenbrink[1]✉, Emmy E. Stigter[1], Tandong Yao[2] and Walter W. Immerzeel[1]

Streamflow in high-mountain Asia is influenced by meltwater from snow and glaciers, and determining impacts of climate change on the region's cryosphere is essential to understand future water supply. Past and future changes in seasonal snow are of particular interest, as specifics at the scale of the full region are largely unknown. Here we combine models with observations to show that regional snowmelt is a more important contributor to streamflow than glacier melt, that snowmelt magnitude and timing changed considerably during 1979–2019 and that future snow meltwater supply may decrease drastically. The expected changes are strongly dependent on the degree of climate change, however, and large variations exist among river basins. The projected response of snowmelt to climate change indicates that to sustain the important seasonal buffering role of the snowpacks in high-mountain Asia, it is imperative to limit future climate change.

Climate change in high-mountain Asia (HMA) has been considerable over the last decades, with significant warming and large areas experiencing wetting or drying (Extended Data Fig. 1). Impacts of climate change on the cryosphere[1] strongly affect the amount and timing of fresh water supplied by the region's natural water towers. This fresh water is used directly and indirectly by millions of people downstream for irrigation, hydroelectric power and consumption[2–5]. Glaciers have responded by generally losing mass[6,7] and as a result have received considerable attention associated with their importance as a water supply[3,5,8] and future changes therein[9–11]. In contrast, past and future relevance of snow to the region's hydrology has been marginally addressed at the scale of HMA, since research has predominantly focused on smaller subregions[3,5,12,13] or on snow properties that provide limited hydrological context such as snow cover[14] or depth[15]. Accurate and detailed information about the amount of water stored in HMA's snowpacks (that is, their snow water equivalent (SWE)) is largely absent or inaccurate at large scale because SWE is notoriously difficult to monitor using remote sensing[16–20]. Nonetheless, to unravel many of the societal and environmental processes that occur in HMA, an improved understanding of the influence of snow on the region's (future) water balance is essential[21–23].

Here we quantify SWE and snowmelt at high spatial resolution in all major river basins[24] of HMA (Fig. 1) and present past and potential future changes in SWE across the entire region in detail by a combining a regional scale snow model with gridded climate data, satellite snow cover observations, a bottom-up elasticity approach and general circulation model (GCM) projections. In the snow model, which operates at 0.05° resolution (~5.7 km), snow accumulation is determined by (a fraction of) precipitation when temperatures are below 2 °C, and snowmelt is parameterized using a positive degree-day approach[25], which is based on air temperature only. Since snowmelt is also controlled by incoming radiation and snowpack thinning can be caused by other processes such as sublimation and wind redistribution[26,27], the melt parameterization is an incomplete representation of the entire snow ablation process. However, given the spatial and temporal scale of this study and the lack of spatially representative input data in HMA to calibrate and validate snow models, it provides the optimal approach. To ensure the most realistic snowmelt given the limitations imposed by data scarcity, we implemented a temporally variable melt rate based on snow albedo[28] and added refreezing and rain-on-snow components. In addition, to account for diurnal and altitudinal variability of snow in the high-mountain regions of HMA, we ran the model at a three-hourly time step and implemented a subgrid routine, which ensures a better representation of the shoulder seasons (that is, the onsets of the snow season and the melting season). We ran the model for the period 1979–2019 and forced it by air temperature and precipitation data from the state-of-the-art European Centre for Medium-Range Weather Forecasts ReAnalysis 5 (ERA5) gridded climate reanalysis[29]. The model was calibrated using 2000–2019 snow cover from Moderate Resolution Imaging Spectroradiometer (MODIS) satellite imagery[30] to correct biases in the reanalysis data (Methods). To account for spatiotemporal uncertainty that is due to the limitations imposed by the model concept and uncertainties in the input forcing, we performed a first-order second-moment uncertainty analysis (Supplementary Methods).

Modelled SWE was validated using in situ measurements of SWE in the Nepalese Himalaya[31,32] and daily snow-depth maps derived from spaceborne Sentinel-1 radar data[15]. Despite—and considering—the obvious scale differences and lack of representation of spatially variable mountainous snowpacks by individual point measurements[33], the in situ measurements are largely in agreement with modelled SWE in both magnitude and timing (Supplementary Fig. 1). The remotely sensed snow-depth observations further endorse model performance, as modelled snow depths are generally in good agreement (Supplementary Fig. 2) as indicated by several model performance metrics (Supplementary Methods).

Distribution and importance of snow

The spatial and temporal distribution of modelled SWE and snowmelt varies considerably over HMA's river basins (Figs. 1 and 2). The basins in the northwest (that is, Syr Darya and Lake Balkash) have a short snow season with most SWE accumulated at the low plains, where snow meltwater is rapidly released in March (Fig. 3). In the lower-latitude basins (that is, Indus, Ganges, Brahmaputra,

[1]Department of Physical Geography, Faculty of Geosciences, Utrecht University, Utrecht, the Netherlands. [2]Institute of Tibetan Plateau Research, Chinese Academy of Sciences, Beijing, China. ✉e-mail: p.d.a.kraaijenbrink@uu.nl

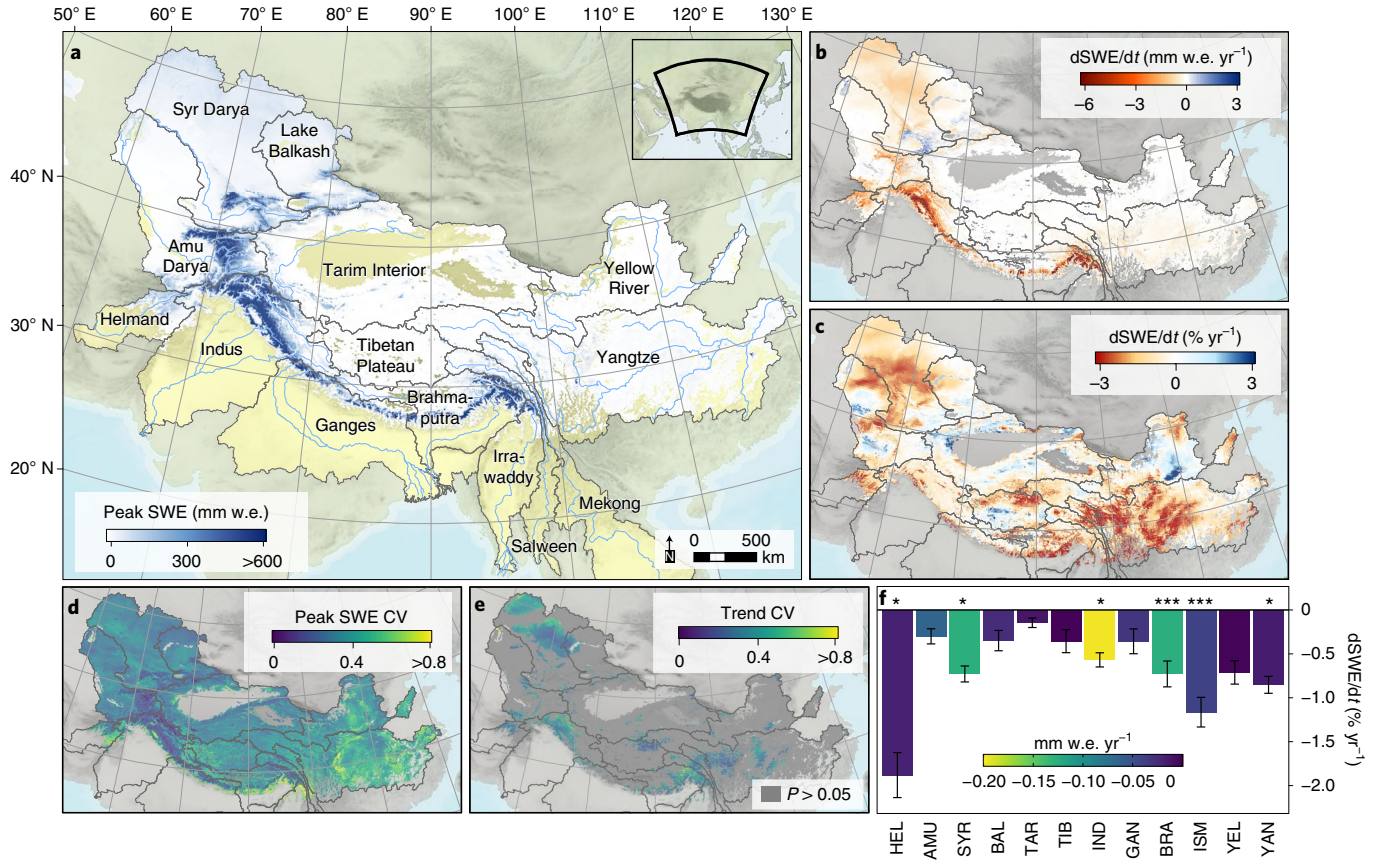

Fig. 1 | SWE and historical absolute and relative trends. a, Overview map of HMA annotated with major rivers and basins[24] and simulated mean annual peak SWE over the period 1979–2019. w.e., water equivalent. **b**,**c**, Absolute (**b**) and relative (**c**) trends in the annual peak SWE over the same period. **d**, Model uncertainty in mean annual peak SWE expressed as coefficient of variation (CV). **e**, Trend uncertainty expressed as CV, with areas of statistically insignificant trends ($P > 0.05$) masked out. **f**, Basin-wide aggregated relative trends in mean annual SWE for snow years (September–August), with trend uncertainty indicated by the error bars (standard deviation) and trend significance denoted by the asterisks (*$P \leq 0.05$; ***$P \leq 0.001$). HEL, Helmand; AMU, Amu Darya; SYR, Syr Darya; BAL, Lake Balkash; TAR, Tarim Interior; TIB, Tibetan Plateau; IND, Indus; GAN, Ganges; BRA, Brahmaputra; ISM, Irrawaddy, Salween and Mekong combined; YEL, Yellow River; YAN, Yangtze.

Irrawaddy, Salween and Mekong) temperatures are higher (Extended Data Fig. 1); hence, snow is mostly present at high elevations (>3,000 m) and melts gradually from low to high elevation (Fig. 3 and Extended Data Fig. 2). Although the Indian monsoon provides copious amounts of moisture to the source areas of the lower-latitude river basins in summer[34], seasonal snowpacks accumulate primarily through winter disturbances[12,35–37]. The Yellow River and Yangtze basins have SWE clustered over multiple elevation ranges and a relatively short snow season of two to three months with an early snowmelt onset in February (Fig. 2). The endorheic basins of Tarim Interior and Tibetan Plateau have snow only at high elevations, with gradual snow meltwater release over a long melt season (Fig. 2). However, these basins have relatively little precipitation and thus comparatively little snowfall. The Amu Darya basin reveals a similar snowmelt season to the basins of Tarim Interior and Tibetan Plateau, but this is mainly caused by the heterogeneous climatic and geographic zones of this river basin.

For the upper basins, defined as the area of a river basin that is above 2,000 m elevation, we find that snowmelt is consistently a more important contributor to basin hydrology than glacier melt (Figs. 2 and 4) (Methods), which is in agreement with recent findings[13]. Although annual glacier melt contribution in the upper basin is respectable in river basins that have large glacierized areas in their source areas (for example, Indus (13.4 ± 1.8%) and Amu Darya (10.0 ± 1.5%)) (Fig. 4), the snowmelt contribution is generally three to five times larger than the glacier melt contribution (Fig. 2) and can even be an order of magnitude larger (for example, in Helmand, Syr Darya and Yellow River). In the southeastern and eastern basins, characterized by summer monsoon precipitation and warmer climates (Extended Data Fig. 1), total meltwater contributions to overall streamflow are limited with upper basin contributions ranging from 28.9 ± 2.0% for Ganges to 7.6 ± 0.6% for Yangtze (Fig. 4). In the more arid west, snow and glacier meltwater are key components of the annual streamflow; for example, in the Indus, Amu Darya and Syr Darya, the combined contributions of snow and glacier meltwater to annual streamflow are 69.1 ± 1.7%, 84.5 ± 1.3% and 59.6 ± 2.2%, respectively (the specific contributions of snowmelt are 55.4 ± 2.4%, 74.5 ± 1.9% and 55.9 ± 2.3%, respectively). This east–west variability in glacier and snowmelt contribution agrees with previous studies[3,38,39], although there are also reports of unusually high snowmelt contributions in the monsoon-dominated upper basins of Ganges (43%) and Brahmaputra (66%) (ref. [13]). It should be noted that glacier melt usually lags snowmelt and continues through summer when the snow storage has been largely depleted. Therefore, glacier melt can be dominant for brief periods during the late melt season[13]. However, rainfall runoff has generally become an important part of the streamflow by that time, reducing the overall importance of snow and glacier meltwater for the water supply[39,40]. Nevertheless, glaciers may become critically important in periods of drought when snowpacks have already melted and rainfall runoff is absent[41].

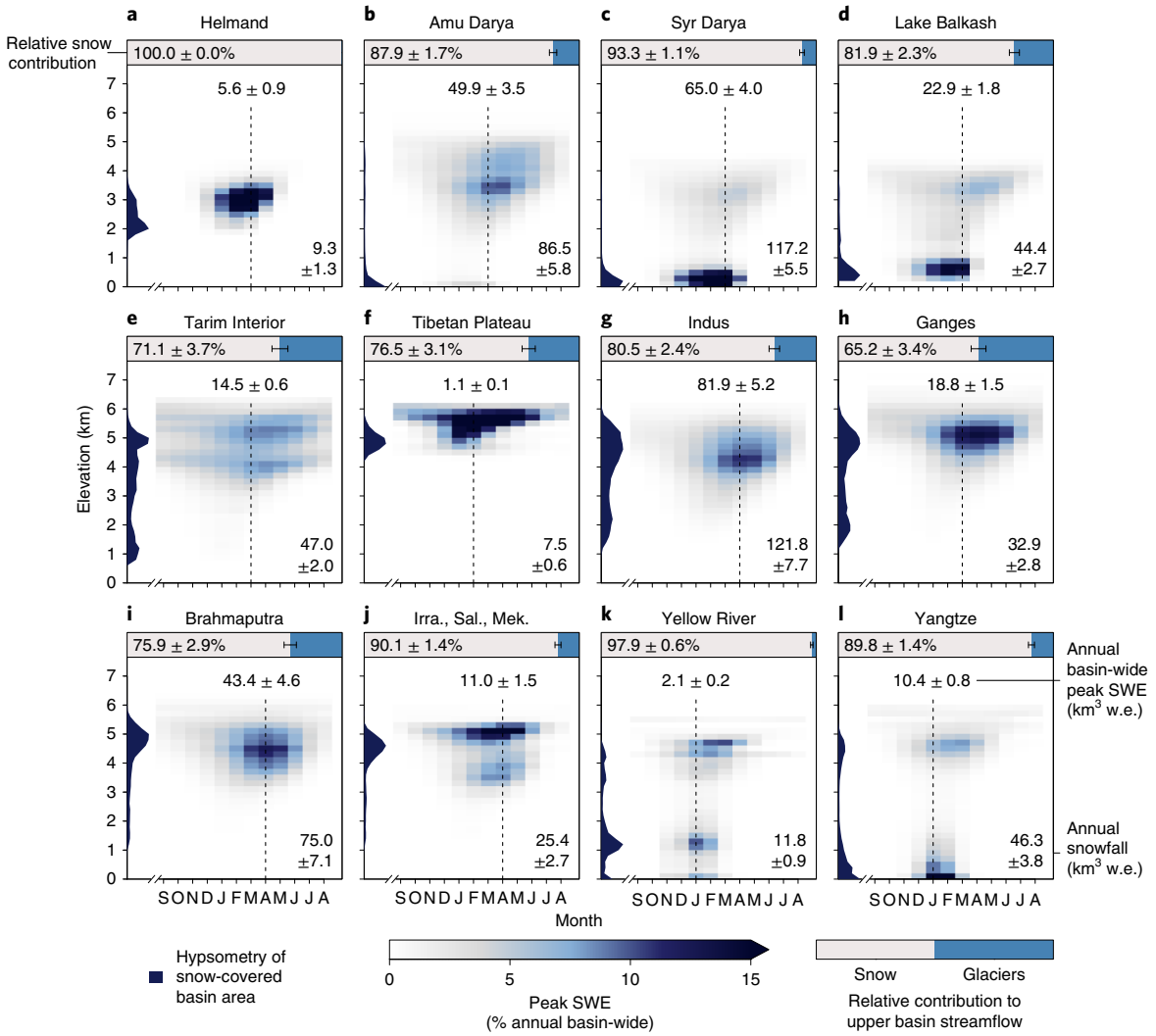

Fig. 2 | SWE climatology for the period 1979–2019. a–l, Monthly peak SWE climatology (sorted September–August) per 200 m elevation band and for each basin normalized by annual basin-wide peak SWE. The month of basin-wide peak SWE is indicated by the dotted line, with the peak SWE magnitude annotated above. The area chart on the left *y* axis shows relative hypsometry for the basin area that experiences at least four days of annual snow cover. The bar on top denotes relative mean annual meltwater contribution (1979–2019) of snow and glaciers for the upper basin (>2,000 m). All uncertainties and error bars indicate the standard deviation. Irra., Sal., Mek., Irrawaddy, Salween and Mekong.

Past changes in snow and snowmelt

Over the period 1979–2019, we estimate significant negative changes in the maximum annual amount of water stored as snow (that is, peak SWE) for large regions in HMA (Fig. 1b,c). Most affected are the northern plains of Syr Darya, Helmand and Indus as well as large parts of central and eastern HMA. Although absolute changes in peak SWE are small for the eastern parts of the arid interior region, such as the Tibetan Plateau and upstream parts of the Brahmaputra, relative changes in peak SWE are largest there, with annual reductions of over 6.0 ± 1.8% for the period 1979–2019. Despite receiving additional precipitation over the last decades, large temperature increases have resulted in significant relative decreases of SWE, in particular on the eastern Tibetan Plateau (Extended Data Fig. 1). Looking at the endorheic Tibetan Plateau Basin as a whole, there has not been a significant reduction of the mean annual snowpack (Fig. 1f). The connected and monsoon-dominated region of the upper Brahmaputra, Irrawaddy, Salween, Mekong and Yangtze Basins, however, is characterized by significant snowpack reductions. From a basin perspective, the strongest relative snowpack change is found in Helmand (−1.9 ± 0.3% yr^{-1}), but due to the limited snowfall in the basin this represents only a relatively small absolute change (−0.02 mm w.e. yr^{-1}). From a seasonal and altitudinal perspective, relative changes are often strongest in the shoulder seasons and at the lower elevations (Supplementary Fig. 3), since the effects of climate change on the shallow snowpacks at these fringes can be relatively immediate. Eventually, these reductions in snow may translate to shorter snow seasons and a rapid associated decrease in albedo, which contributes to elevation-dependent warming feedbacks[42,43]. In some basins, SWE shows significant increases in the upper 1,000 m of the basin because of increased winter precipitation (Supplementary Fig. 3), such as in the Lake Balkash and Tarim Interior basins, but these trends are relatively small (<0.1% yr^{-1}).

There has been substantial shortening of the snowmelt season and changes in timing of the snow meltwater peak between the periods 1979–1999 and 1999–2019 (Fig. 3 and Extended Data Fig. 2). For instance, in the region for which we classify the climatological snowmelt hydrograph as Short Season (Helmand, Syr Darya and Lake Balkash; Fig. 3) the average snowmelt peak for 1999–2019 occurs ~5 days earlier than for 1979–1999, comprises 87.2 ± 8.3%

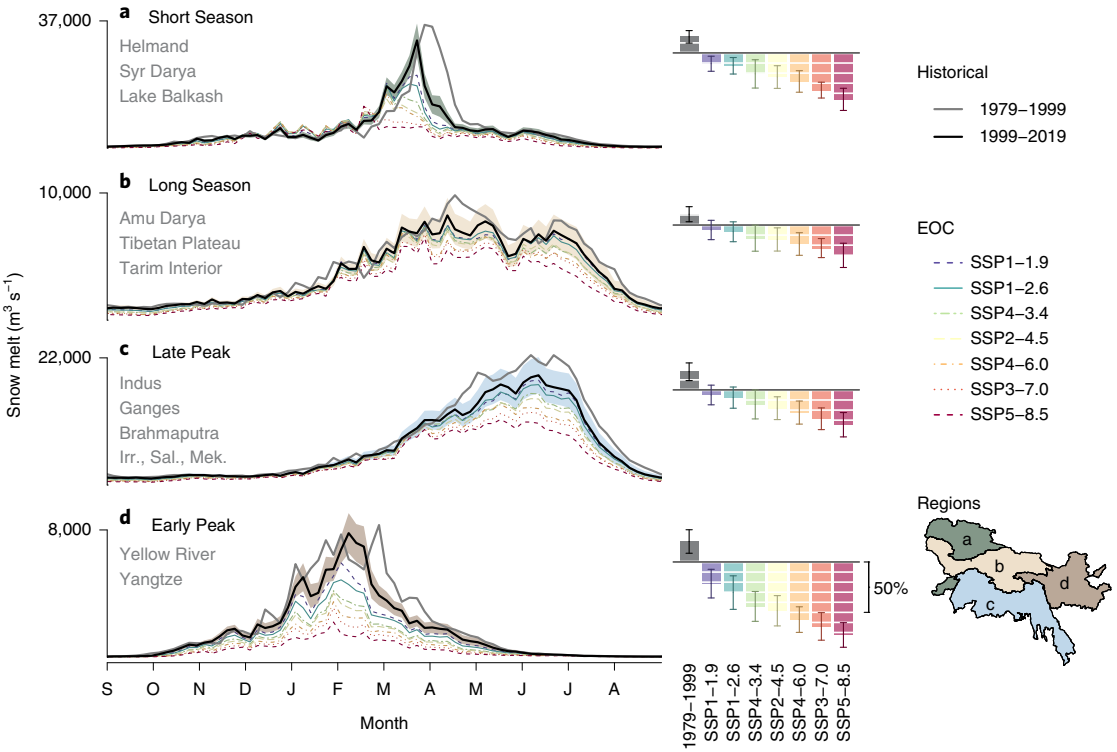

Fig. 3 | Snowmelt hydrographs for four melt regimes. a–d, Climatological snowmelt hydrographs for the four distinct snowmelt regimes present in HMA (Extended Data Fig. 2) for historical (1979–1999) and present day (1999–2019) periods, sorted September–August. The dashed lines are associated with model runs forced with mean climate projections for Climate Model Intercomparison Project Phase 6 (CMIP6) shared socioeconomic pathways (SSP)–representative concentration pathways (RCP) model ensembles (Supplementary Table 1) for the end of century (EOC; 2071–2100). The coloured shading indicates the 95% confidence interval for the present day. The colour key for the regions is given in the lower right corner of the figure. The adjacent bar plots indicate historical and projected future differences in annual snowmelt with respect to present day, where each block represents 10%. The error bars indicate one standard deviation in the model response and, for the future projections, represent combined uncertainty of the snow model and SSP–RCP ensembles. The hydrographs are based on five-day-sum climatology. Details of the region map are presented in Fig. 1a.

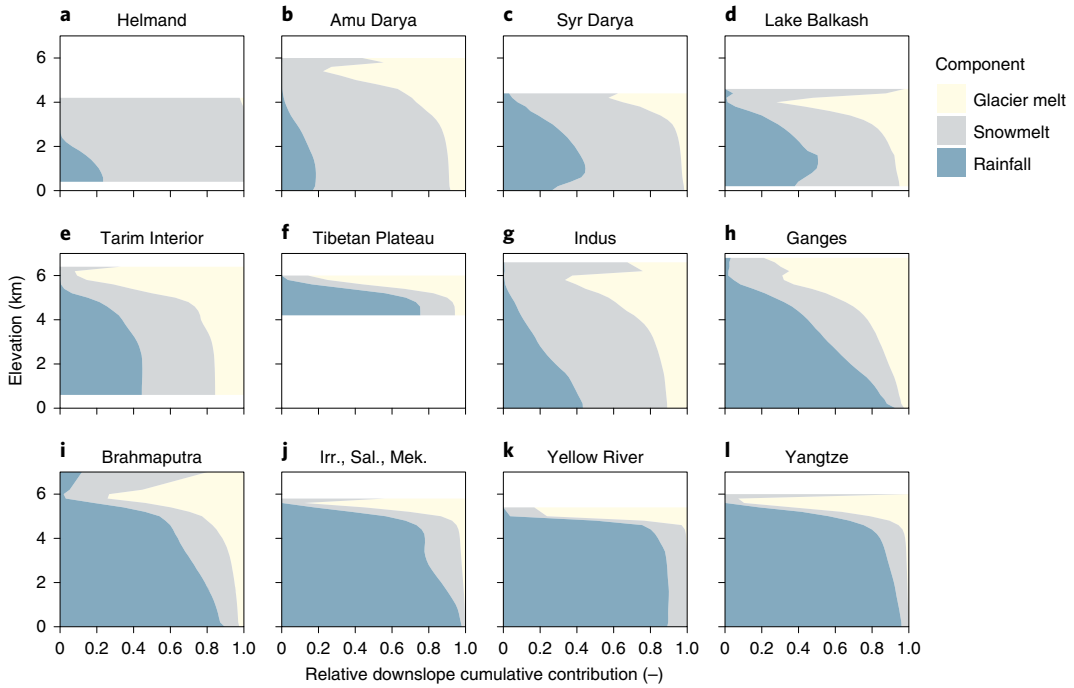

Fig. 4 | Relative contributions of rainfall, snowmelt and glacier melt. a–l, Relative contributions of rainfall, snowmelt and glacier melt for the period 1979–2019 over the entire elevation range of each river basin. The contributions are cumulated from high to low elevation.

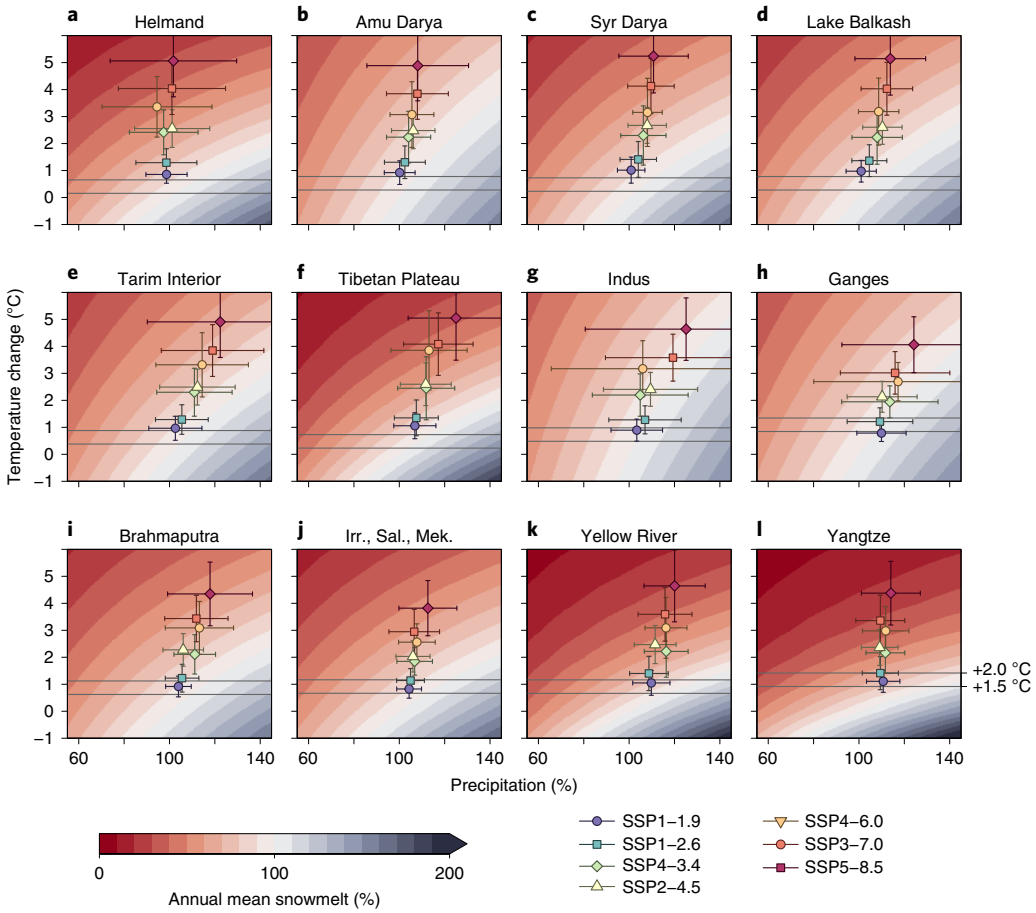

Fig. 5 | Response of snowmelt to changes in precipitation and temperature. a–l, Relative difference for all basins in climatological annual mean snowmelt between reference period 2000–2019 and the same period with superimposed changes in precipitation and temperature. The points and whiskers denote mean and standard deviation of the CMIP6 SSP–RCP model ensembles (Supplementary Table 1) for the EOC (2071–2100). The lower and upper solid lines indicate the relative position, respectively, of +1.5 °C and +2.0 °C scenarios[1] with respect to pre-industrial climate (1851–1880).

of the original volume and reverts to lower snowmelt rates more quickly. In the region that is characterized by an Early Peak hydrograph (Yellow River and Yangtze; Fig. 3), a considerable shortening of the melt season by almost a month is observed, caused by both a delayed onset and early snowpack depletion. Interestingly, the largely monsoon-dominated region classified as Late Peak (Indus, Ganges, Brahmaputra, Irrawaddy, Salween and Mekong; Fig. 3) shows a delay of the snow meltwater peak, albeit one that is small and coincident with an uncertain peak reduction of 17.8 ± 20.7%. All regions have experienced a clear decline in terms of total annual snow meltwater (14.7 ± 6.2%, 11.0 ± 7.4%, 18.1 ± 8.3% and 20.8 ± 11.1% for the Short Season, Long Season, Late Peak and Early Peak regions, respectively; Fig. 3). This is mainly explained by a change in snow–rain partitioning and increased snowmelt rates due to increasing temperatures together with a decrease in overall precipitation in most regions (Extended Data Fig. 1).

Sensitivity and future projections

The sensitivity of annual mean snowmelt to changes in temperature and precipitation shows large variations across HMA (Fig. 5). The eastern basins of Yellow River and Yangtze are most sensitive and lose 17 ± 4% °C^{-1} on average. Moreover, the temperature dependency of snowmelt here is non-linear and considerably stronger initially (Extended Data Fig. 3). By contrast, the Indus and Ganges basins are comparatively insensitive to changes in temperature with 7 ± 1% °C^{-1} on average and show an approximately linear relation between changes in temperature and snowmelt. However, the Indus basin in particular has a total volume of snow that is much larger than in Yellow River and Yangtze (Fig. 2). Despite the relative insensitivity of Indus's snowpacks to temperature change, absolute decreases in annual snowmelt volume are therefore still substantial at 8.5 ± 1.1 km^3 °C^{-1}. Differences in sensitivity of annual mean snowmelt, annual mean SWE and annual peak SWE can be distinct and vary considerably among the basins (Fig. 5 and Extended Data Fig. 3), which can be attributed mainly to spatio-climatic and hypsometric differences.

GCM ensemble mean future temperature and precipitation changes for the EOC (2071–2100), as determined for seven experiments of CMIP6 (Supplementary Table 1) defined by combinations of SSPs and RCPs[44], show that most parts of HMA, with the exception of Helmand basin, are projected to have increases in precipitation (Fig. 5). The SSP–RCP ensemble standard deviations are large, however, particularly for precipitation, as there are considerable differences between the projections of the individual GCMs in this climatologically complex region[45]. The increases in precipitation may partly counteract reduced snowfall due to rising temperatures and could have considerable effect in basins that show a relatively low sensitivity of their snowpacks to changes in temperature (Extended Data Fig. 3) and for which substantial increases in precipitation are projected, such as the Ganges basin (Fig. 5). The snow season may both shorten and intensify in such cases, with potential implications for avalanche risks, for example. However, the specific future snow

climatology will also depend on how synoptic weather patterns may shift, on changes in the relative strength of westerly disturbances[46] and monsoon systems[47], and on how these effects conspire to change the seasonality of future precipitation[12].

Model runs forced by SSP–RCP ensemble mean monthly temperature and precipitation for the EOC (Methods) reveal that the magnitude and timing of snow meltwater release will continue to change in the future. Further attenuation of the snowmelt hydrograph, shortening of the snowmelt season and shifts in the timing of the snowmelt peak are projected (Fig. 3). The optimistic SSP1–2.6 scenario reveals relatively modest changes compared to the present day (1999–2019), with reductions in annual snow meltwater of 12.7 ± 7.9% (Short Season), 6.7 ± 9.8% (Long Season), 7.6 ± 10.7% (Late Peak), 30.4 ± 16.9% (Early Peak) and 11.1 ± 5.4% (entire HMA). Of all basins, the snow-dominated Indus basin shows the least change in snowmelt under this scenario with a loss of only 2.6 ± 10.6% (Extended Data Fig. 4). Differences to the SSP5–8.5 scenario are distinct, as a region-wide loss in annual snow meltwater of 40.5 ± 6.5% is projected under this extreme 'worst-case' scenario. Moreover, under SSP5–8.5, disappearance of snow on the northern plains of the Short Season region will result in large reductions in the snowmelt peak (61.2 ± 13.1%) and annual snowmelt (46.1 ± 11.4%) with respect to present day (Fig. 3). In the Long Season and Late Peak regions, annual snowmelt is expected to be reduced by 30.1 ± 12.1% and 34.6 ± 12.4%, and in the Early Peak region, by as much as 72.5 ± 11.9%. The other SSP–RCP scenarios fall between the extremes (Fig. 3 and Extended Data Fig. 4), with the exception of the highly optimistic SSP1–1.9, which is intended to limit warming by 2100 to 1.5 °C above pre-industrial conditions[48] and exhibits the smallest reductions of snow meltwater. Achievement of the 1.5 °C or 2.0 °C targets set by the 2015 Paris agreement, which have received considerable societal and scientific attention in recent years[49], would clearly benefit snow meltwater supply compared to more extreme scenarios, as only moderate region-wide losses of 5.6 ± 3.4% and 11.2 ± 5.1%, respectively, would be expected by the EOC (Fig. 5, Supplementary Table 2 and Extended Data Fig. 3).

The projected future snowmelt shows distinctly negative trends with increasing radiative forcing for all river basins (Extended Data Fig. 4), with reductions ranging from 8.2 ± 3.8% (SSP1–1.9) to 41.5 ± 3.6% (SSP5–8.5) on average by the EOC. Losses of glacier melt (Methods), on the other hand, are stronger (ranging from 31.8 ± 7.0% to 41.2 ± 9.4% on average) and are often relatively constant or even decrease with an increase in forcing (Extended Data Fig. 4). This is caused by differences in the timing of increased glacial meltwater release[9,10,50] caused by (1) stabilizing temperatures and small precipitation increases under low forcing (that is, reduced excess melt due to stabilizing glacier mass balances and only small mass turnover increases) and (2) continued temperature rise and strong precipitation increases under stronger forcing (that is, sustained excess melt and increased mass turnover despite decreasing glacier surface areas). Henceforth, from both a cryospheric and hydrologic perspective the relative importance of snow for HMA's rivers will increase. Absolute drops in snowmelt volume generally exceed those of glacier melt, as there is more snowmelt than glacier melt (Figs. 2 and 4), and the decline of snowmelt therefore has considerably larger impacts on downstream meltwater supply than that of glaciers for most future scenarios (Extended Data Fig. 4).

Conclusions

Snowmelt is important in many parts of HMA, much more so than glacier melt, and the supply of snow meltwater to many of the region's large rivers has reduced over the last four decades because of climate change. Snowmelt contributions to streamflow will continue to fall irrespective of future climate scenario, but projected magnitudes are strongly related to the degree of warming, drying or wetting. Under an optimistic scenario such as limiting temperature rise above pre-industrial conditions to 2.0 °C, only a moderate 11.2 ± 5.1% of snow meltwater would be lost with respect to present day. More realistic (SSP2–4.5) or worst-case scenarios (SSP5–8.5) may prove to be decisive for downstream snow meltwater availability, with region-wide reductions of 21.9 ± 4.5% and 40.5 ± 3.6%, respectively, and up to 51.3 ± 11.8% and 74.4 ± 9.4% respectively for specific basins. Limiting the degree of climate change in this century will undoubtedly provide decisive benefits in terms of future water supply in HMA's snow-dominated river basins but will require immediate societal and political action.

Online content

Any methods, additional references, Nature Research reporting summaries, source data, extended data, supplementary information, acknowledgements, peer review information; details of author contributions and competing interests; and statements of data and code availability are available at https://doi.org/10.1038/s41558-021-01074-x.

Received: 24 January 2020; Accepted: 12 May 2021;
Published online: 24 June 2021

References

1. IPCC *Special Report on the Ocean and Cryosphere in a Changing Climate* (WMO, 2019).
2. Viviroli, D., Dürr, H. H., Messerli, B., Meybeck, M. & Weingartner, R. Mountains of the world, water towers for humanity: typology, mapping, and global significance. *Water Resour. Res.* **43**, W07447 (2007).
3. Immerzeel, W. W., van Beek, L. P. H. & Bierkens, M. F. P. Climate change will affect the Asian water towers. *Science* **328**, 1382–1385 (2010).
4. Immerzeel, W. W. et al. Importance and vulnerability of the world's water towers. *Nature* **577**, 364–369 (2019).
5. Biemans, H. et al. Importance of snow and glacier meltwater for agriculture on the Indo-Gangetic Plain. *Nat. Sustain.* **2**, 594–601 (2019).
6. Brun, F., Berthier, E., Wagnon, P., Kääb, A. & Treichler, D. A spatially resolved estimate of high mountain Asia glacier mass balances, 2000–2016. *Nat. Geosci.* **10**, 668–673 (2017).
7. Shean, D. E. et al. A systematic, regional assessment of high mountain Asia glacier mass balance. *Front. Earth Sci.* **7**, 1–19 (2020).
8. Nie, Y. et al. Glacial change and hydrological implications in the Himalaya and Karakoram. *Nat. Rev. Earth Environ.* **2**, 91–106 (2021).
9. Kraaijenbrink, P. D. A., Bierkens, M. F. P., Lutz, A. F. & Immerzeel, W. W. Impact of a global temperature rise of 1.5 degrees Celsius on Asia's glaciers. *Nature* **549**, 257–260 (2017).
10. Huss, M. & Hock, R. Global-scale hydrological response to future glacier mass loss. *Nat. Clim. Change* **8**, 135–140 (2018).
11. Rounce, D. R., Hock, R. & Shean, D. E. Glacier mass change in high mountain Asia through 2100 using the open-source Python glacier evolution model (PyGEM). *Front. Earth Sci.* **7**, 1–20 (2020).
12. Kapnick, S. B., Delworth, T. L., Ashfaq, M., Malyshev, S. & Milly, P. C. D. Snowfall less sensitive to warming in Karakoram than in Himalayas due to a unique seasonal cycle. *Nat. Geosci.* **7**, 834–840 (2014).
13. Armstrong, R. L. et al. Runoff from glacier ice and seasonal snow in High Asia: separating melt water sources in river flow. *Reg. Environ. Change* **19**, 1249–1261 (2019).
14. Hammond, J. C., Saavedra, F. A. & Kampf, S. K. Global snow zone maps and trends in snow persistence 2001–2016. *Int. J. Climatol.* **38**, 4369–4383 (2018).
15. Lievens, H. et al. Snow depth variability in the Northern Hemisphere mountains observed from space. *Nat. Commun.* **10**, 4629 (2019).
16. Dozier, J., Bair, E. H. & Davis, R. E. Estimating the spatial distribution of snow water equivalent in the world's mountains. *Wiley Interdiscip. Rev. Water* **3**, 461–474 (2016).
17. Bormann, K. J., Brown, R. D., Derksen, C. & Painter, T. H. Estimating snow-cover trends from space. *Nat. Clim. Change* **8**, 924–928 (2018).
18. Smith, T. & Bookhagen, B. Changes in seasonal snow water equivalent distribution in high mountain Asia (1987 to 2009). *Sci. Adv.* **4**, 1–8 (2018).
19. Smith, T. & Bookhagen, B. Assessing multi-temporal snow-volume trends in high mountain Asia from 1987 to 2016 using high-resolution passive microwave data. *Front. Earth Sci.* **8**, 1–13 (2020).
20. Thapa, A. & Muhammad, S. Contemporary snow changes in the Karakoram region attributed to improved MODIS data between 2003 and 2018. *Water* **12**, 2681 (2020).
21. Huss, M. et al. Toward mountains without permanent snow and ice. *Earths Future* **5**, 418–435 (2017).

22. Livneh, B. & Badger, A. M. Drought less predictable under declining future snowpack. *Nat. Clim. Change* **10**, 452–458 (2020).
23. Qin, Y. et al. Agricultural risks from changing snowmelt. *Nat. Clim. Change* **10**, 459–465 (2020).
24. Lehner, B. & Grill, G. Global river hydrography and network routing: baseline data and new approaches to study the world's large river systems. *Hydrol. Process.* **27**, 2171–2186 (2013).
25. Hock, R. Temperature index melt modelling in mountain areas. *J. Hydrol.* **282**, 104–115 (2003).
26. Stigter, E. E. et al. The importance of snow sublimation on a Himalayan glacier. *Front. Earth Sci.* **6**, 108 (2018).
27. Sarangi, C. et al. Dust dominates high-altitude snow darkening and melt over high-mountain Asia. *Nat. Clim. Change* **10**, 1045–1051 (2020).
28. Brock, B. W., Willis, I. C. & Sharp, M. J. Measurement and parameterization of albedo variations at Haut Glacier d'Arolla, Switzerland. *J. Glaciol.* **46**, 675–688 (2000).
29. *ERA5 Reanalysis* (ECMWF, 2017).
30. Hall, D. K., Riggs, G. A., Foster, J. L. & Kumar, S. V. Development and evaluation of a cloud-gap-filled MODIS daily snow-cover product. *Remote Sens. Environ.* **114**, 496–503 (2010).
31. Putkonen, J. K. Continuous snow and rain data at 500 to 4400 m altitude near Annapurna, Nepal, 1999–2001. *Arct. Antarct. Alp. Res.* **36**, 244–248 (2004).
32. Kirkham, J. D. et al. Near real-time measurement of snow water equivalent in the Nepal Himalayas. *Front. Earth Sci.* **7**, 1–18 (2019).
33. Grünewald, T. & Lehning, M. Are flat-field snow depth measurements representative? A comparison of selected index sites with areal snow depth measurements at the small catchment scale. *Hydrol. Process.* **29**, 1717–1728 (2015).
34. Ceglar, A., Toreti, A., Balsamo, G. & Kobayashi, S. Precipitation over monsoon Asia: a comparison of reanalyses and observations. *J. Clim.* **30**, 465–476 (2017).
35. Cannon, F., Carvalho, L. M. V., Jones, C. & Norris, J. Winter westerly disturbance dynamics and precipitation in the western Himalaya and Karakoram: a wave-tracking approach. *Theor. Appl. Climatol.* **125**, 27–44 (2016).
36. Thapa, K., Endreny, T. A. & Ferguson, C. R. Atmospheric rivers carry non-monsoon extreme precipitation into Nepal. *J. Geophys. Res. Atmospheres* **123**, 5901–5912 (2018).
37. Ménégoz, M., Gallée, H. & Jacobi, H. W. Precipitation and snow cover in the Himalaya: from reanalysis to regional climate simulations. *Hydrol. Earth Syst. Sci.* **17**, 3921–3936 (2013).
38. Bookhagen, B. & Burbank, D. W. Toward a complete Himalayan hydrological budget: spatiotemporal distribution of snowmelt and rainfall and their impact on river discharge. *J. Geophys. Res. Earth Surf.* **115**, 1–25 (2010).
39. Lutz, A. F., Immerzeel, W. W., Shrestha, A. B. & Bierkens, M. F. P. Consistent increase in High Asia's runoff due to increasing glacier melt and precipitation. *Nat. Clim. Change* **4**, 587–592 (2014).
40. Wulf, H., Bookhagen, B. & Scherler, D. Differentiating between rain, snow, and glacier contributions to river discharge in the western Himalaya using remote-sensing data and distributed hydrological modeling. *Adv. Water Resour.* **88**, 152–169 (2016).
41. Pritchard, H. D. Asia's shrinking glaciers protect large populations from drought stress. *Nature* **569**, 649–654 (2019).
42. Pepin, N. et al. Elevation-dependent warming in mountain regions of the world. *Nat. Clim. Change* **5**, 424–430 (2015).
43. Palazzi, E., Filippi, L. & von Hardenberg, J. Insights into elevation-dependent warming in the Tibetan Plateau–Himalayas from CMIP5 model simulations. *Clim. Dyn.* **48**, 3991–4008 (2017).
44. Eyring, V. et al. Overview of the Coupled Model Intercomparison Project Phase 6 (CMIP6) experimental design and organization. *Geosci. Model Dev.* **9**, 1937–1958 (2016).
45. Jiang, J., Zhou, T., Chen, X. & Zhang, L. Future changes in precipitation over Central Asia based on CMIP6 projections. *Environ. Res. Lett.* **15**, 054009 (2020).
46. Ridley, J., Wiltshire, A. & Mathison, C. More frequent occurrence of westerly disturbances in Karakoram up to 2100. *Sci. Total Environ.* **468–469**, S31–S35 (2013).
47. Hasson, S. U., Pascale, S., Lucarini, V. & Böhner, J. Seasonal cycle of precipitation over major river basins in South and Southeast Asia: a review of the CMIP5 climate models data for present climate and future climate projections. *Atmos. Res.* **180**, 42–63 (2016).
48. Rogelj, J. et al. Scenarios towards limiting global mean temperature increase below 1.5 °C. *Nat. Clim. Change* **8**, 325–332 (2018).
49. IPCC *Special Report on Global Warming of 1.5 °C* (eds Masson-Delmotte, V. et al.) (WMO, 2018).
50. Immerzeel, W. W., Pellicciotti, F. & Bierkens, M. F. P. Rising river flows throughout the twenty-first century in two Himalayan glacierized watersheds. *Nat. Geosci.* **6**, 742–745 (2013).

Methods

Snow model. *Model concept.* In this study, snowmelt is parameterized using a temperature index (TI) melt model[25], which is based on the well-established, high correlation between air temperature (T) and snowmelt. In general, TI models have been shown to perform well in large-scale analyses and outperform simplified energy balance models[51,52]. Physically based multi-layer models that solve the full energy balance of the snowpack and account for snow metamorphism can be more accurate at small spatial and temporal scale when sufficient and accurate input data are available[53], but at the scale of the entire HMA, the necessary input data are unavailable or inaccurate. Moreover, increased model complexity does not guarantee high model performance[54–56]. Increasing the number of snow processes in a model leads to an increased number of parameterizations and, hence, increases of free parameters and required meteorological variables. This results in problematic model calibration as well as increased input uncertainty due to high spatial variability of meteorological variables in complex terrain. As the TI model is based on T only, which is widely available and relatively easily downscaled and/or interpolated spatially[25], it is particularly suited to modelling snowmelt across HMA. Extensions of the TI model exist that include, for example, incoming shortwave radiation to better incorporate changes in albedo[57,58]. However, these approaches also require data that are unavailable or inaccurate at regional scale, similarly to full energy balance models, with negative impacts on the accuracy of snow simulations[59–61].

We extended the standard daily TI model with a number of important improvements: (1) the use of a three-hourly time step, (2) mixed precipitation phase based on two temperature thresholds, (3) time-variable melt factor as a function of number of days without snow, (4) inclusion of water storage and refreezing in the snowpack and (5) accounting for subgrid variability using 100 m elevation bands within a 0.05° model grid cell.

To distinguish between solid and liquid precipitation, we use threshold temperatures. When T is subzero ($T_{\mathrm{solid}}=0\,^{\circ}\mathrm{C}$), all precipitation is assumed to be solid, and when T is greater than 2 °C (T_{liquid}), all precipitation is liquid. In between these thresholds, we linearly interpolate to determine the fraction of P that is P_{solid} (ref. [62]):

$$P_{\mathrm{solid},t}=\begin{cases} P_t & \text{if } T_t < T_{\mathrm{solid},t},\\ 0 & \text{if } T_t > T_{\mathrm{liquid},t},\\ \left(1-\frac{T_t}{T_{\mathrm{liquid},t}-T_{\mathrm{solid},t}}\right)P_t & \text{if } T_{\mathrm{solid},t}\le T_t\le T_{\mathrm{liquid},t}\end{cases} \tag{1}$$

When $T\ge 0\,^{\circ}\mathrm{C}$, we use T (in °C) for time step (t) in conjunction with a melt rate given by a degree-day melt factor ($\mathrm{DDF_M}$) to determine potential snowmelt[25]. Additionally, to account for accelerated melt caused by rain-on-snow events[63] that can occur in the shoulder seasons, the melt energy of the rainfall is added to the potential melt, for which we assume an isothermal 0 °C snowpack. Actual snowmelt in mm (M_{S}) is limited by the amount of snow present as snow storage (S_{S}):

$$M_{\mathrm{S},t}=\begin{cases}\min\left(S_{\mathrm{S},t-1},\ T_t\mathrm{DDF_M}\Delta t+\frac{T_tC_{\mathrm{p}}(P_t-P_{\mathrm{solid},t})}{L_{\mathrm{f}}}\right) & \text{if } T\ge 0\\ 0 & \text{if } T<0\end{cases} \tag{2}$$

where Δt is the length of a time step in days, C_{p} the specific heat capacity (4.18 $\mathrm{J\,g^{-1}\,^{\circ}C^{-1}}$) and L_{f} the latent heat of fusion (333.55 $\mathrm{J\,g^{-1}}$) of water. The snow storage at time step t is then given by:

$$S_{\mathrm{S},t}=S_{\mathrm{S},t-1}+P_{\mathrm{solid},t}-M_{\mathrm{S},t} \tag{3}$$

$\mathrm{DDF_M}$ for snow can vary over time and seasons[64], which is primarily caused by a decline in snow albedo (α) as the snowpack ages, for example due to snow metamorphism-induced changes in grain size and deposition of light-absorbing impurities[65–67]. Since snow metamorphism is a main driver in albedo change and metamorphism rates vary spatially and temporally for different climates, determining snowpack albedo from time or season alone is not accurate[28,64]. To allow for a dependency of the albedo decay on the variable rate of change in snowpack characteristics across HMA, we parameterize snow albedo using the positive degree-day sum (PDD) since last snowfall[28] (that is, the accumulated daily maximum temperatures above 0 °C):

$$\alpha_t=0.713-0.112\log_{10}\mathrm{PDD}_t \tag{4}$$

To translate α into $\mathrm{DDF_M}$, it is inversely scaled to melt rates of 4 ($\alpha=0.85$) and 9 ($\alpha=0.40$) $\mathrm{mm\,^{\circ}C^{-1}\,d^{-1}}$ for fresh and aged snow[68,69], respectively.

Most snowmelt percolates the snowpack and runs off or infiltrates the soil underneath, but part of the meltwater is stored in the snowpack itself. When temperatures fall below 0 °C, this meltwater may refreeze and form ice layers in or at the base of the snowpack[70]. The magnitude of refreezing in HMA's catchments can be considerable[71,72], and it can delay meltwater release[73]. To account for refreezing, we accumulate snow meltwater in a snow water storage (S_{W}). The capacity is limited to 10% of the snowpack mass, which is equivalent to 1.4–4.6% of the snowpack volume for a bulk snow density ranging between 150 and 550 $\mathrm{kg\,m^{-3}}$ and is representative for alpine snowpacks[73–75]:

$$S_{\mathrm{W},t}=\min\left(0.1S_{\mathrm{S},t},\ S_{\mathrm{W},t-1}+M_{\mathrm{S},t}\right) \tag{5}$$

When $T<0\,^{\circ}\mathrm{C}$, liquid water present in the snowpack can refreeze following a negative degree-day approach and using a rate of 1 $\mathrm{mm\,^{\circ}C^{-1}\,d^{-1}}$ ($\mathrm{DDF_R}$) (ref. [76]). Refrozen meltwater is defined as ice storage (S_{I}):

$$S_{\mathrm{I},t}=S_{\mathrm{I},t-1}+\min\left(S_{\mathrm{W},t-1},\ -T_{T<0,t}\mathrm{DDF_R}\Delta t\right) \tag{6}$$

Melt of the snowpack (M_{S}) and related reduction in meltwater storage capacity results in the discharge of both snow meltwater and any overcapacity of the water storage (Q_{S}) when $T>0\,^{\circ}\mathrm{C}$. Any existing ice storage is set to melt (M_{I}), similarly to the snow storage (equation (2)), after the snow has fully melted:

$$Q_{\mathrm{S},t}=\begin{cases} M_{\mathrm{S},t}-\Delta S_{\mathrm{W}} & \text{if } S_{\mathrm{S},t}>0\\ M_{\mathrm{I},t} & \text{if } S_{\mathrm{S},t}=0 \text{ and } S_{\mathrm{S},t-1}=0\\ M_{\mathrm{S},t}-\Delta S_{\mathrm{W}}+\min\left(S_{\mathrm{I},t-1},\ T_{T\ge 0,t}\mathrm{DDF_M}\Delta t-M_{\mathrm{S},t}\right) & \text{if } S_{\mathrm{S},t}=0 \text{ and } S_{\mathrm{S},t-1}>0\end{cases} \tag{7}$$

Domain. To study seasonal snow across HMA, we apply the model in a domain bounded by all 14 major river basins in the region (Fig. 1), which were derived from the HydroSHEDS dataset[24]. For the basin-scale analyses in this study, we group the southeastern basins of Irrawaddy, Salween and Mekong into one unit, since the upstream areas of these basins with snowfall are comparatively small and have similar climates and responses.

Although the model can run at any spatial and temporal resolution, we apply it at 0.05° (~5.7 km) with a three-hourly time step. By running at a sub-daily timescale, we account for diurnal variations in melt and snowfall, which are, for most regions, particularly in effect during initial and final (that is, melt) stages of the snow season when daily average T is close to 0 °C and daily maximum temperature exceeds 0 °C. Diurnal cycles of snowfall, melt and refreezing can play an important role in the timing of snow meltwater release and are important to include to accurately model snow[71,73,76].

We limit our analysis to model grid cells that have at least four days of snow cover per year on average for the time period 2000–2019 to reduce noise and to limit computation time. Snow cover days were determined using the cloud-masked 500 m resolution daily snow cover product of MODIS Terra[77] (MOD10A1 v6) in Google Earth Engine[78] (GEE) for September 2000 to August 2019 (that is, the reference period, which here is considered present day). To construct daily binary snow cover maps, we apply a Normalized Difference Snow Index threshold of 0.1 instead of the global reference value[77] of 0.4, since this value has been shown to be more accurate for the large arid (interior) regions of our domain and does not significantly negatively influence results elsewhere[79]. For the entire analysis, water bodies were masked out using the MOD44W v6 water mask dataset[80].

Subgrid routine. A model grid of 0.05° is too coarse to capture altitudinal variation in the snowpack in the high relief areas of HMA. We therefore implemented a subgrid routine in which for each model grid cell the TI model is run separately for 100 m elevation bands (z) determined from Shuttle Radar Topography Mission (SRTM) elevation data[81]. The subgrid routine is performed at the resolution of MODIS snow cover product (500 m) using spatially aggregated SRTM elevation. Although the vertical accuracy of SRTM data are reduced in very steep areas due to the presence of large outliers and voids[82], this has limited effects on the results of our model because of the use of aggregated elevation data and the relatively small planimetric surface area represented by those areas. Furthermore, output at the grid level is determined by weighted aggregation of the results for the elevation bands, which further reduces the effects of potential errors in individual elevation bands. T_z is lapsed with respect to the input T series using dynamic monthly temperature lapse rates calculated from climatological land surface temperatures for the reference period, which were calculated in GEE using the 1 km resolution MODIS eight-day land surface temperature product[83] (MOD11A2 v6) after cloud masking. For each model grid cell, the lapse rates are calculated using linear regression between SRTM elevation and land surface temperature for a 0.25° window centred around the cell. We constrain lapse rates to the range −0.0120 to $-0.0020\,^{\circ}\mathrm{C\,m^{-1}}$, use regression results only when they are significant ($P\le 0.05$) and fall back to a default lapse rate of $-0.0065\,^{\circ}\mathrm{C\,m^{-1}}$ otherwise.

For some subgrid elevations, T_z is (almost) always negative. These bands occur at very high elevation, where perennial snow is present and snowmelt is not the dominant ablation type. At these high-elevation sites, snowpack evolution is likely dominated by (wind-blown) sublimation, wind redistribution and avalanching[26,84,85]. As the TI model depends on positive T to parameterize melt, it cannot operate accurately in these cases, as snow would continue to accumulate unrealistically. Since this negatively affects the output aggregated to the model grid, we force a long-term stable snowpack in these elevation bands by using a

high-pass filter with a one-year window on $S_{S,z}$ and add a baseline $S_{S,z}$ of half the grid cell's annual precipitation. This approach retains temporally dynamic snow, as snow accumulates naturally and a constant snow removal by the aforementioned processes is simulated. We allow filtered $S_{S,z}$ to contribute to S_S as normal, but removal of snow by this procedure does not contribute to snowmelt (Q_S). Overall, this procedure affects only 1.1% of the model domain and 3.1% of the model grid cells.

Forcing. To force the snow model, we use T and P data from the state-of-the-art 31 km resolution ERA5 gridded climate reanalysis[29], aggregated to three-hourly input from the original hourly resolution to reduce the computational requirements of the snow model. The currently available ERA5 data span the period 1979–2019 and thus allow for analysis of changes over recent decades. Previous studies have indicated that ERA-Interim (ref. [86]), which is ERA5's predecessor and used an older version of the same assimilation scheme, better represents high-altitude precipitation than other large-scale reanalysis products[87,88]. ERA5 has improved spatial resolution and uses additional input datasets and instruments that were not ingested before, resulting in reduced biases compared to ERA-Interim (ref. [89]), and thus presumably provides better representation and definition of (mountain) precipitation. ERA5 has been shown to improve land surface analyses[90], improve surface radiation budgets[91,92] and provide better wind and temperature over sea[93] compared to ERA-Interim. A comparative study of 26 precipitation products for the conterminous United States[94] showed that ERA5 is the most accurate of the reanalysis products, although not without biases. Moreover, it provided a marked improvement over ERA-Interim, particularly in the mountainous west. ERA5-based hydrological modelling performance was therefore found to be largely equivalent to using observations over most of North America[89]. Although there are not yet any explicit studies of ERA5 performance over the larger HMA, it has been shown that ERA5 has mean monthly precipitation represented better than ERA-Interim on the eastern Tibetan Plateau[95] but that there are still considerable biases, particularly in the wet season[96,97]. To assess the impacts of using different forcing datasets on the results of the snow model, we performed a comparison of five gridded climate products (Supplementary Methods).

Calibration. T biases often exist in reanalysis data, including ERA5[89,95,98,99]. As T is a key component of the TI model, it is important to bias-correct the input T fields using independent data. We perform this in a model calibration procedure in which we minimize the difference between modelled and observed snow persistence (that is, the fraction of time a location is snow-covered). We obtained observed snow persistence from monthly snow cover climatology derived from cloud-masked MOD10A1 data for the reference period. T bias is determined at the model grid by a numerical non-linear least squares minimization between the modelled and observed snow persistence of the subgrid elevation bands. This calibration approach (1) reduces remaining spatial and altitudinal discrepancies between the 0.05° model and the 31 km ERA5 grids and (2) improves upon the limited capability of the TI approach to properly model spatial variability in snow that results from topographic effects[25], as it aids to partially embed other processes that affect evolution of the snowpack, such as sublimation and wind redistribution, in the temperature signal. The calibrated temperature fields show that 60% of absolute biases are lower than 5 °C and 80% are lower than 10 °C. High biases are mostly found in the arid interior areas such as the Tibetan Plateau and Tarim Interior where (wind-blown) sublimation is likely to play a large role. Since these snow loss processes are not explicitly modelled in the TI approach, temperature must be raised to simulate snow seasons with lengths similar to those observed. This does mean that the accuracy of the seasonal dynamics of snow in these areas may be reduced. We note, however, that actual biases between ERA5 T and station data on the Tibetan Plateau were reported to reach up to 8 °C in winter months[95], and that it is therefore likely that only a fraction of the bias stems from limitations of the snow model itself.

Elasticity and future projections. The sensitivity of SWE and snowmelt to changes in T and P was estimated by superimposing combinations of changes (deltas) in these two variables to the (calibrated) ERA5 time series for the reference period 2000–2019. For each combination of ΔT (°C) and ΔP (%), we performed a separate model run and calculated change statistics with respect to the reference run ($\Delta T = 0$ °C and $\Delta P = 0$%). Combinations were constructed using a ΔT sequence from −1 °C to 6 °C with steps of 1 °C and a ΔP sequence from −40% to +40% with steps of 10%. SWE and snowmelt responses that fall in between these deltas were calculated using bilinear interpolation.

To put the sensitivity of future changes in SWE and snowmelt in perspective, we compared the results with GCM ensemble T and P changes for the EOC (2071–2100). These were determined from GCM runs ($n = 143$) for seven experiments of CMIP6[44] (Supplementary Table 1), which are defined by combinations of SSPs and RCPs. To obtain the ensemble T and P changes for the EOC, we calculated, for all GCMs separately, monthly climatological ΔT and ΔP between the reference period (2000–2019) and the EOC to account for biases among the different GCMs. Statistics per SSP–RCP ensemble then provided ensemble mean monthly ΔT and ΔP and their standard deviations. Separate model runs in which for each SSP–RCP experiment the monthly spatial fields of climatological ensemble mean ΔT and ΔP were superimposed on the reference climatology were performed to determine the state of snowmelt in the EOC and differences with the present day. A comparison of the snow model output as forced with CMIP6 with model output from initial runs that were forced using CMIP5 (ref. [100]) RCP ensembles[9] is shown in Supplementary Fig. 4.

Non-linear changes in the processes and feedbacks related to the snowpack energy balance due to climate change can affect the translation of degree days to snowmelt using a DDF (refs. [25,64]). To assess the impacts of this uncertainty in DDF_M on future projections, we performed a DDF sensitivity analysis (Supplementary Methods).

Melt contributions. *Contributions of snow, glaciers and rain.* To estimate relative annual contributions of snowmelt to river runoff in HMA with respect to glacier melt, we calculated absolute contributions of glacier melt, snowmelt and rainfall runoff for every model grid cell. Since the aim of this comparison was to compare relative contributions of snow and glacier melt, we did not employ a full hydrological model and disregarded hydrological processes such as infiltration, groundwater storage, relative contributions to river baseflow, transition times, anthropogenic water usage and so on.

We estimated glacier melt contribution by calculating the two main components of glacier melt discharge (Q_G): melt related to mass turnover in equilibrium state ($Q_{G,eq}$) and the excess that is due to glacier imbalance ($Q_{G,ex}$). ERA5 precipitation (P) and glacier data from the Randolph Glacier Inventory version 5 (RGI5; ref. [101]) were combined to determine $Q_{G,eq}$. We consider all precipitation that falls on the glacierized area (A_G) (that is, both the accumulation and ablation zone) to contribute to the glacier melt discharge. $Q_{G,ex}$ is calculated using glacier area and individual glacier mass balances (B_G) derived from stereo satellite imagery over the period 2000–2018 (ref. [7]). Although glaciers can extend beyond a single model pixel, we set discharge to occur in the cell of the glacier terminus, determined from RGI5 glacier outlines[101] and SRTM elevation[81]. Total glacier melt is then calculated by:

$$Q_G = Q_{G,eq} + Q_{G,ex} = A_G P + A_G B_G \quad (8)$$

To calculate annual snowmelt discharge (Q_S) for this comparison of contributions, we used P_{solid} as reported by our model. Since all on-glacier precipitation is included as glacier discharge, we corrected the snowfall in a grid cell by the fraction of glacierized area to obtain snowmelt discharge:

$$Q_S = P_{solid}\left(1 - \frac{A_G}{A}\right) \quad (9)$$

where A is the total area of a grid cell.

Rainfall runoff is determined using P by correcting for ERA5 evaporation (E), rainfall on glaciers and snowfall:

$$Q_R = (P - E) \times \left(1 - \frac{A_G}{A}\right) - Q_S \quad (10)$$

Although sublimation constitutes a loss term in a basin's water balance, similarly to included evaporation, we do not specifically account for it because it is difficult to quantify accurately for such a large region and requires multi-parameter parameterizations or energy balance models that, for reasons discussed above, are infeasible at the scale of this study and impossible to validate with currently available data. We acknowledge that sublimation may play an important role[26] and that snowmelt contribution with respect to rainfall could decrease if it were included. With respect to glacier melt, however, differences will be small, as on-glacier snow experiences largely the same processes as off-glacier snow.

Future glacier melt. Future projections of glacier mass and area loss in HMA were performed for all glaciers larger than 0.4 km² using a mass-balance gradient glacier model[9] to determine the relative change in glacier meltwater contribution for the EOC (2071–2100) compared to the present day (2000–2019). After running the model for each of the 143 CMIP6 runs (Supplementary Table 1) separately, we determined SSP–RCP ensemble mean changes by the EOC for each glacier ($n = 33{,}587$) individually for (1) the average remaining glacier area, (2) the change in glacier mass over 2071–2100, which together with area provides the mean glacier mass balance and (3) the change in precipitation with respect to the reference period. Using equation (8), we then calculated SSP–RCP ensemble mean EOC glacier melt discharge and its differences compared to the reference period and aggregated results to the river basin scale. For the glacier model runs performed here, the initial glacier boundary conditions and reference P and T used originally[9] were updated to match the reference period and data used in this study (2000–2019 and ERA5, respectively). The starting year of the glacier model runs was adapted accordingly to 2010. Combined model and climate projection uncertainty was determined using a Monte Carlo approach, as in the original study[9].

Data availability

Data generated by this study are available online for download at https://doi.org/10.5281/zenodo.4715786. This includes daily 0.05° grids for 1979–2019, EOC

projections and the bottom-up elasticity output for both SWE and snowmelt. Additional model outputs and derivatives are available from the authors upon request. Pre-processed input data to run the snow model are available at https://doi.org/10.5281/zenodo.4715955. Precipitation and temperature fields from ERA5 reanalysis data[29] used in this study are available from the Copernicus Climate Data Store at https://cds.climate.copernicus.eu/. CMIP6 data[44] used in this study are available at https://pcmdi.llnl.gov/CMIP6/. MODIS snow cover data[77] are available at https://nsidc.org/data/MOD10A1/versions/6, land surface temperature data[83] at https://doi.org/10.5067/MODIS/MOD11A2.006 and water mask[80] at https://doi.org/10.5067/MODIS/MOD44W.006. SRTM elevation data[81] are available at https://srtm.csi.cgiar.org/. HydroSHEDS basin outlines[24] are available from https://www.hydrosheds.org/. Glacier outlines from the Randolph Glacier Invertory[101] are available at https://www.glims.org/RGI/.

Code availability

Code for the snow model presented in this study is available at https://doi.org/10.5281/zenodo.4715953. Code for the glacier model[9] is available at https://doi.org/10.5281/zenodo.2548689. Other code is available from the authors upon request.

References

51. Huss, M. & Hock, R. A new model for global glacier change and sea-level rise. *Front. Earth Sci.* https://doi.org/10.3389/feart.2015.00054 (2015).
52. Comola, F. et al. Scale-dependent effects of solar radiation patterns on the snow-dominated hydrologic response. *Geophys. Res. Lett.* **42**, 3895–3902 (2015).
53. Sicart, J. E., Hock, R. & Six, D. Glacier melt, air temperature, and energy balance in different climates: the Bolivian tropics, the French Alps, and northern Sweden. *J. Geophys. Res. Atmos.* **113**, D24113 (2008).
54. Essery, R., Morin, S., Lejeune, Y. & B Ménard, C. A comparison of 1701 snow models using observations from an alpine site. *Adv. Water Resour.* **55**, 131–148 (2013).
55. Magnusson, J. et al. Evaluating snow models with varying process representations for hydrological applications. *Water Resour. Res.* **51**, 2707–2723 (2015).
56. Avanzi, F. et al. Model complexity and data requirements in snow hydrology: seeking a balance in practical applications. *Hydrol. Process.* **30**, 2106–2118 (2016).
57. Pellicciotti, F. et al. An enhanced temperature-index glacier melt model including the shortwave radiation balance: development and testing for Haut Glacier d'Arolla, Switzerland. *J. Glaciol.* **51**, 573–587 (2005).
58. Heynen, M., Pellicciotti, F. & Carenzo, M. Parameter sensitivity of a distributed enhanced temperature-index melt model. *Ann. Glaciol.* **54**, 311–321 (2013).
59. Franz, K. J., Hogue, T. S. & Sorooshian, S. Operational snow modeling: addressing the challenges of an energy balance model for National Weather Service forecasts. *J. Hydrol.* **360**, 48–66 (2008).
60. Slater, A. G., Barrett, A. P., Clark, M. P., Lundquist, J. D. & Raleigh, M. S. Uncertainty in seasonal snow reconstruction: relative impacts of model forcing and image availability. *Adv. Water Resour.* **55**, 165–177 (2013).
61. Lapo, K. E., Hinkelman, L. M., Raleigh, M. S. & Lundquist, J. D. Impact of errors in the downwelling irradiances on simulations of snow water equivalent, snow surface temperature, and the snow energy balance. *Water Resour. Res.* **51**, 1649–1670 (2015).
62. Maussion, F. et al. The open global glacier model (OGGM) v1.1. *Geosci. Model Dev.* **12**, 909–931 (2019).
63. Cohen, J., Ye, H. & Jones, J. Trends and variability in rain-on-snow events. *Geophys. Res. Lett.* **42**, 7115–7122 (2015).
64. Livneh, B., Xia, Y., Mitchell, K. E., Ek, M. B. & Lettenmaier, D. P. Noah LSM Snow model diagnostics and enhancements. *J. Hydrometeorol.* **11**, 721–738 (2010).
65. Dozier, J. & Painter, T. H. Multispectral and hyperspectral remote sensing of alpine snow properties. *Annu. Rev. Earth Planet. Sci.* **32**, 465–494 (2004).
66. Gautam, R., Hsu, N. C., Lau, W. K.-M. & Yasunari, T. J. Satellite observations of desert dust-induced Himalayan snow darkening. *Geophys. Res. Lett.* **40**, 988–993 (2013).
67. Painter, T. H., Skiles, S. M., Deems, J. S., Brandt, W. T. & Dozier, J. Variation in rising limb of Colorado River snowmelt runoff hydrograph controlled by dust radiative forcing in snow. *Geophys. Res. Lett.* **45**, 797–808 (2018).
68. Singh, P., Kumar, N. & Arora, M. Degree-day factors for snow and ice for Dokriani Glacier, Garhwal Himalayas. *J. Hydrol.* **235**, 1–11 (2000).
69. Braithwaite, R. J. Temperature and precipitation climate at the equilibrium-line altitude of glaciers expressed by the degree-day factor for melting snow. *J. Glaciol.* **54**, 437–444 (2008).
70. Pfeffer, W. T. & Humphrey, N. F. Formation of ice layers by infiltration and refreezing of meltwater. *Ann. Glaciol.* **26**, 83–91 (1998).
71. Saloranta, T. et al. A model setup for mapping snow conditions in high-mountain Himalaya. *Front. Earth Sci.* **7**, 1–18 (2019).
72. Stigter, E. E. et al. Energy and mass balance dynamics of the seasonal snowpack at two high-altitude sites in the Himalaya. *Cold Reg. Sci. Technol.* **183**, 103233 (2021).
73. Samimi, S. & Marshall, S. J. Diurnal cycles of meltwater percolation, refreezing, and drainage in the supraglacial snowpack of Haig Glacier, Canadian Rocky Mountains. *Front. Earth Sci.* **5**, 1–15 (2017).
74. Heilig, A. et al. Seasonal and diurnal cycles of liquid water in snow—measurements and modeling. *J. Geophys. Res. Earth Surf.* **120**, 2139–2154 (2015).
75. Wever, N. et al. Verification of the multi-layer SNOWPACK model with different water transport schemes. *Cryosphere* **9**, 2271–2293 (2015).
76. Stigter, E. E., Wanders, N., Saloranta, T. M., Shea, J. M. & Bierkens, M. F. P. Assimilation of snow cover and snow depth into a snow model to estimate snow water equivalent and snowmelt runoff in a Himalayan catchment. *Cryosphere* **11**, 1647–1664 (2017).
77. Hall, D. K. & Riggs, G. A. *MODIS/Terra Snow Cover Daily L3 Global 500m SIN Grid, Version 6* (NASA National Snow and Ice Data Center Distributed Active Archive Center, accessed 6 December 2019); https://doi.org/10.5067/MODIS/MOD10A1.006
78. Gorelick, N. et al. Google Earth Engine: planetary-scale geospatial analysis for everyone. *Remote Sens. Environ.* **202**, 18–27 (2017).
79. Zhang, H. et al. Ground-based evaluation of MODIS snow cover product V6 across China: implications for the selection of NDSI threshold. *Sci. Total Environ.* **651**, 2712–2726 (2019).
80. Carroll, M. L. et al. *MOD44W MODIS/Terra Land Water Mask Derived from MODIS and SRTM L3 Global 250m SIN Grid V006* (NASA EOSDIS Land Processes DAAC, accessed 5 November 2019); https://doi.org/10.5067/MODIS/MOD44W.006
81. Farr, T. et al. The shuttle radar topography mission. *Rev. Geophys.* **45**, RG2004 (2007).
82. Mukul, M., Srivastava, V., Jade, S. & Mukul, M. Uncertainties in the Shuttle Radar Topography Mission (SRTM) heights: insights from the Indian Himalaya and Peninsula. *Sci. Rep.* **7**, 41672 (2017).
83. Wan, Z., Hook, S. & Hulley, G. *MOD11A2 MODIS/Terra Land Surface Temperature/Emissivity 8-Day L3 Global 1km SIN Grid V006* (NASA EOSDIS Land Processes DAAC, accessed 5 November 2019); https://doi.org/10.5067/MODIS/MOD11A2.006
84. Wagnon, P. et al. Seasonal and annual mass balances of Mera and Pokalde glaciers (Nepal Himalaya) since 2007. *Cryosphere* **7**, 1769–1786 (2013).
85. Litt, M. et al. Glacier ablation and temperature indexed melt models in the Nepalese Himalaya. *Sci. Rep.* **9**, 5264 (2019).
86. Dee, D. P. et al. Toward a consistent reanalysis of the climate system. *Bull. Am. Meteorol. Soc.* **95**, 1235–1248 (2014).
87. Palazzi, E., Von Hardenberg, J. & Provenzale, A. Precipitation in the Hindu-Kush Karakoram Himalaya: observations and future scenarios. *J. Geophys. Res. Atmos.* **118**, 85–100 (2013).
88. Immerzeel, W. W., Wanders, N., Lutz, A. F., Shea, J. M. & Bierkens, M. F. P. Reconciling high-altitude precipitation in the upper Indus basin with glacier mass balances and runoff. *Hydrol. Earth Syst. Sci.* **19**, 4673–4687 (2015).
89. Tarek, M., Brissette, F. P. & Arsenault, R. Evaluation of the ERA5 reanalysis as a potential reference dataset for hydrological modelling over North America. *Hydrol. Earth Syst. Sci.* **24**, 2527–2544 (2020).
90. Albergel, C. et al. ERA-5 and ERA-Interim driven ISBA land surface model simulations: which one performs better? *Hydrol. Earth Syst. Sci.* **22**, 3515–3532 (2018).
91. Huang, J., Rikus, L. J., Qin, Y. & Katzfey, J. Assessing model performance of daily solar irradiance forecasts over Australia. *Sol. Energy* **176**, 615–626 (2018).
92. Urraca, R. et al. Evaluation of global horizontal irradiance estimates from ERA5 and COSMO-REA6 reanalyses using ground and satellite-based data. *Sol. Energy* **164**, 339–354 (2018).
93. Graham, R. M., Hudson, S. R. & Maturilli, M. Improved performance of ERA5 in Arctic gateway relative to four global atmospheric reanalyses. *Geophys. Res. Lett.* **46**, 6138–6147 (2019).
94. Beck, H. E. et al. Daily evaluation of 26 precipitation datasets using Stage-IV gauge-radar data for the CONUS. *Hydrol. Earth Syst. Sci.* **23**, 207–224 (2019).
95. Orsolini, Y. et al. Evaluation of snow depth and snow cover over the Tibetan Plateau in global reanalyses using in situ and satellite remote sensing observations. *Cryosphere* **13**, 2221–2239 (2019).
96. Jiang, Q. et al. Evaluation of the ERA5 reanalysis precipitation dataset over Chinese Mainland. *J. Hydrol.* **595**, 125660 (2020).
97. Chen, Y. et al. Spatial performance of multiple reanalysis precipitation datasets on the southern slope of central Himalaya. *Atmos. Res.* **250**, 105365 (2021).
98. Betts, A. K., Chan, D. Z. & Desjardins, R. L. Near-surface biases in ERA5 over the Canadian Prairies. *Front. Environ. Sci.* **7**, 207–224 (2019).

99. Wang, C., Graham, R. M., Wang, K., Gerland, S. & Granskog, M. A. Comparison of ERA5 and ERA-Interim near-surface air temperature, snowfall and precipitation over Arctic sea ice: effects on sea ice thermodynamics and evolution. *Cryosphere* **13**, 1661–1679 (2019).
100. Taylor, K. E., Stouffer, R. J. & Meehl, G. A. An overview of CMIP5 and the experiment design. *Bull. Am. Meteorol. Soc.* **93**, 485–498 (2012).
101. Pfeffer, W. T. et al. The Randolph Glacier Inventory: a globally complete inventory of glaciers. *J. Glaciol.* **60**, 537–552 (2014).

Acknowledgements

This study was financially supported by the Strategic Priority Research Program of the Chinese Academy of Sciences within the Pan-Third Pole Environment framework (grant agreement no. XDA20100300), by the European Research Council under the European Union's Horizon 2020 research and innovation programme (grant agreement no. 676819) and by the Netherlands Organization for Scientific Research under the Innovational Research Incentives Scheme VIDI (grant agreement 016.181.308). We thank H. Lievens for providing the snowdepth data prior to publication and J. Norris for providing the High Asia high-resolution WRF downscaling that was developed by the Climate Variations and Change research group at the University of California Santa Barbara.

Author contributions

P.D.A.K., W.W.I. and T.Y. designed the study; P.D.A.K. performed all analyses and wrote the manuscript with contributions and suggestions from E.E.S., T.Y. and W.W.I.; and P.D.A.K., W.W.I. and E.E.S. developed the snow model concept.

Competing interests

The authors declare no competing interests.

Additional information

Extended data is available for this paper at https://doi.org/10.1038/s41558-021-01074-x.

Supplementary information The online version contains supplementary material available at https://doi.org/10.1038/s41558-021-01074-x.

Correspondence and requests for materials should be addressed to P.D.A.K.

Peer review information *Nature Climate Change* thanks Bodo Bookhagen, Yukiko Hirabayashi and the other, anonymous, reviewer(s) for their contribution to the peer review of this work.

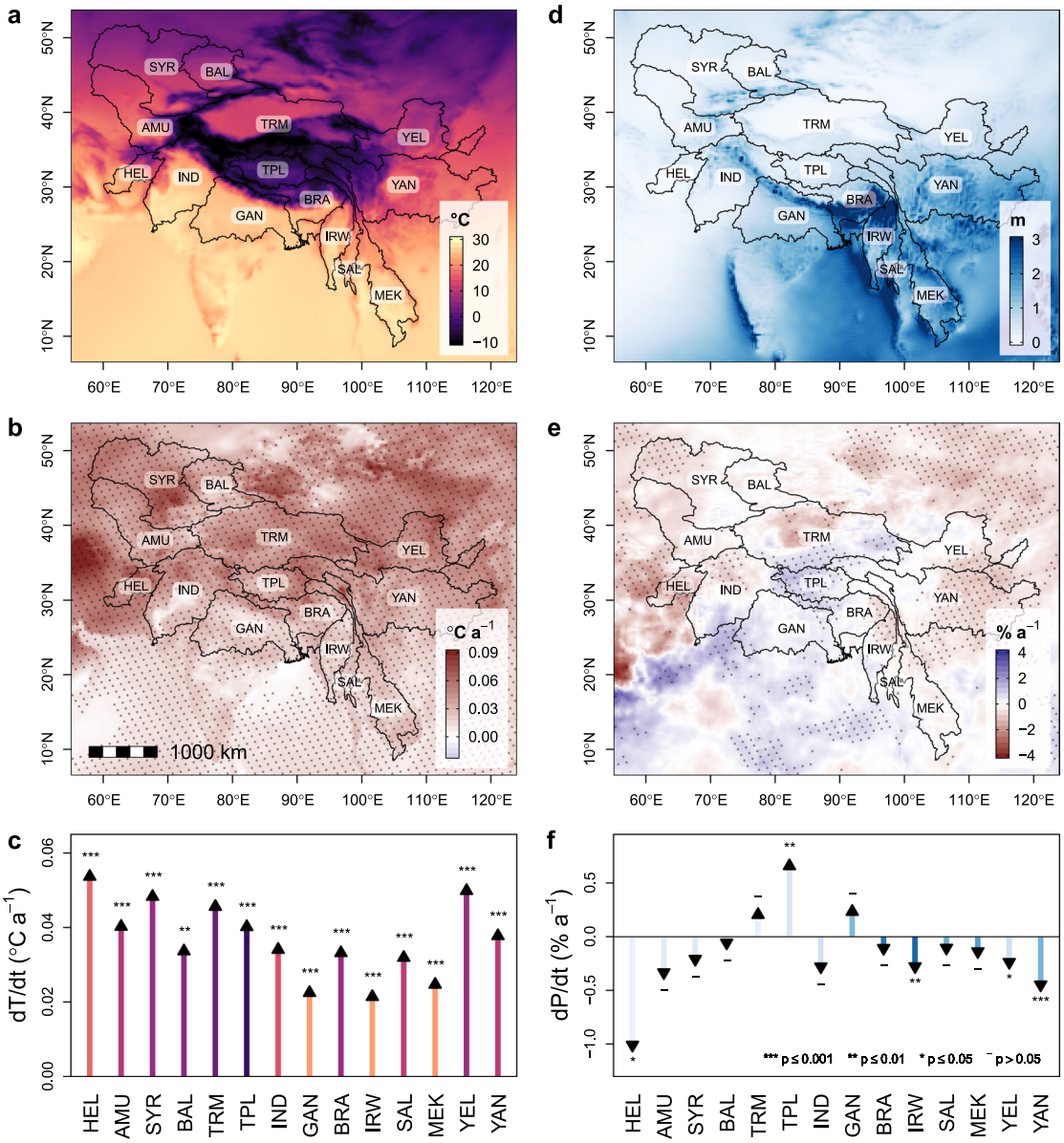

Extended Data Fig. 1 | ERA5 temperature and precipitation. 2-m temperature climatology (**a**), trends in annual mean 2-metre temperature (**a**), and trends in basin-averaged annual 2-m temperature (**c**). Annual cumulative precipitation (**d**), trends in annual precipitation (**e**), and trends in basin-averaged annual precipitation (**f**). The dot overlay in the trend maps (**b**, **e**) indicates areas where trends are significant ($p \leq 0.05$). The colours in the bar plots (**c**, **f**) indicate basin-average temperature and precipitation climatology, and correspond to the colour scales of panel **a** and **d**, respectively. The climatologies and trends of all panels are determined for the period 1979–2019 from the ERA5 gridded reanalysis dataset[29].

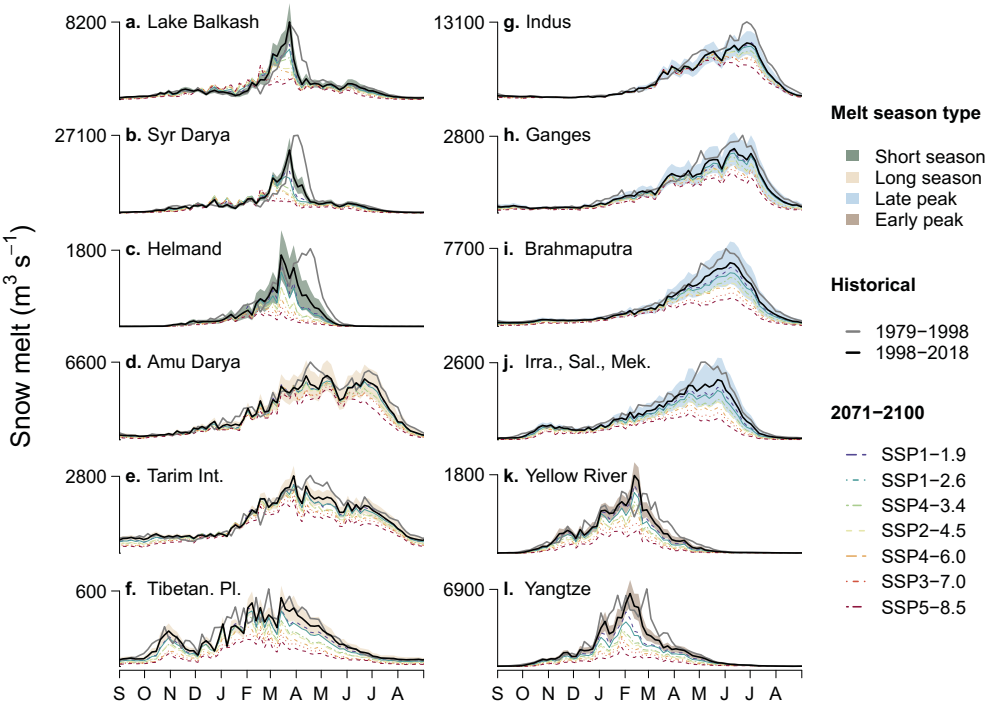

Extended Data Fig. 2 | Snowmelt hydrographs for all river basins. Snowmelt hydrographs for the historical (1979–1999) and present day (1999–2019) periods for individual river basins (**a-l**). Shading indicates the 95% confidence interval for the present-day hydrograph. The colour of the shading indicates one of four identified melt season types (Fig. 3). The dashed lines are hydrographs associated with model runs forced with ensemble mean climate projections for the SSP-RCP experiments within CMIP6[44] for the end of century (2071–2100). All hydrographs are based on average five-day-sum climatologies.

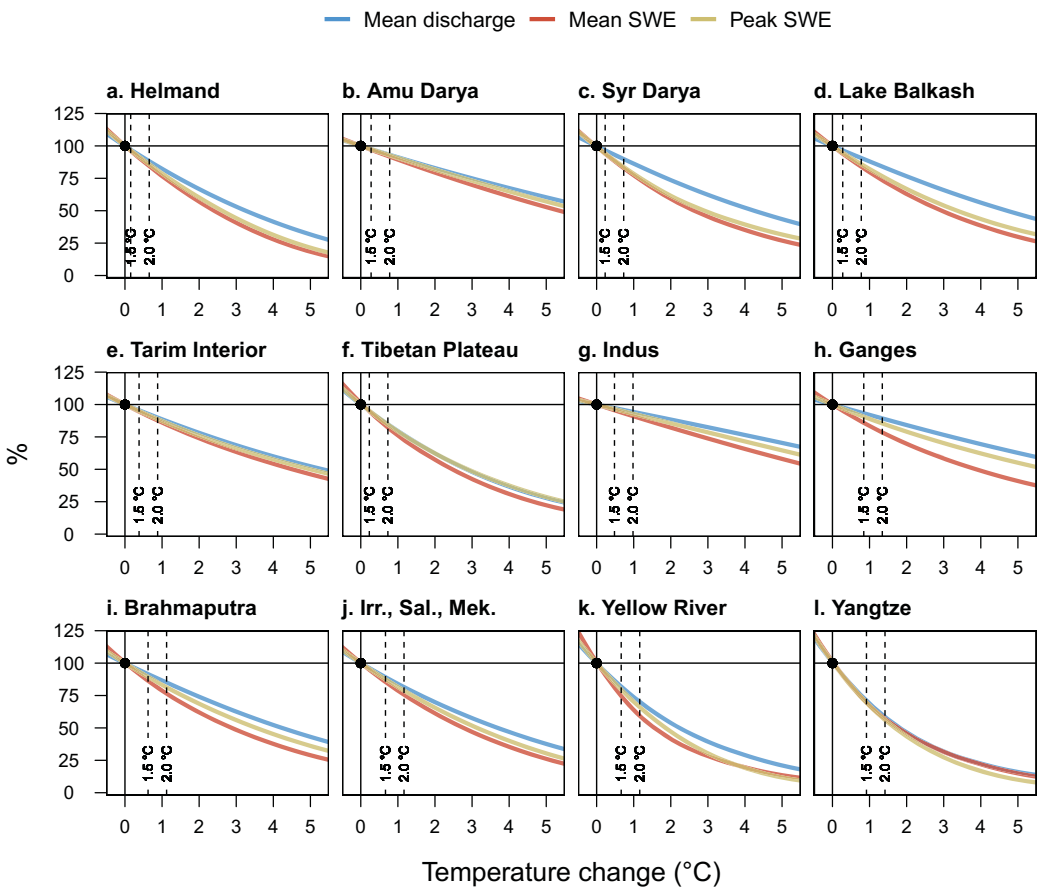

Extended Data Fig. 3 | Sensitivity of snow water equivalent and snowmelt to temperature change. Relative change in the basin-wide mean annual snowmelt, mean annual SWE and peak SWE under changing temperatures with respect to the reference period (2000–2019) for all basins (**a-l**). The dashed vertical lines indicate the relative position of 1.5 °C and 2.0 °C temperature rise scenarios[1] with respect to pre-industrial climate (1851–1880), determined per basin from entire CMIP6 ensemble (Supplementary Table 1).

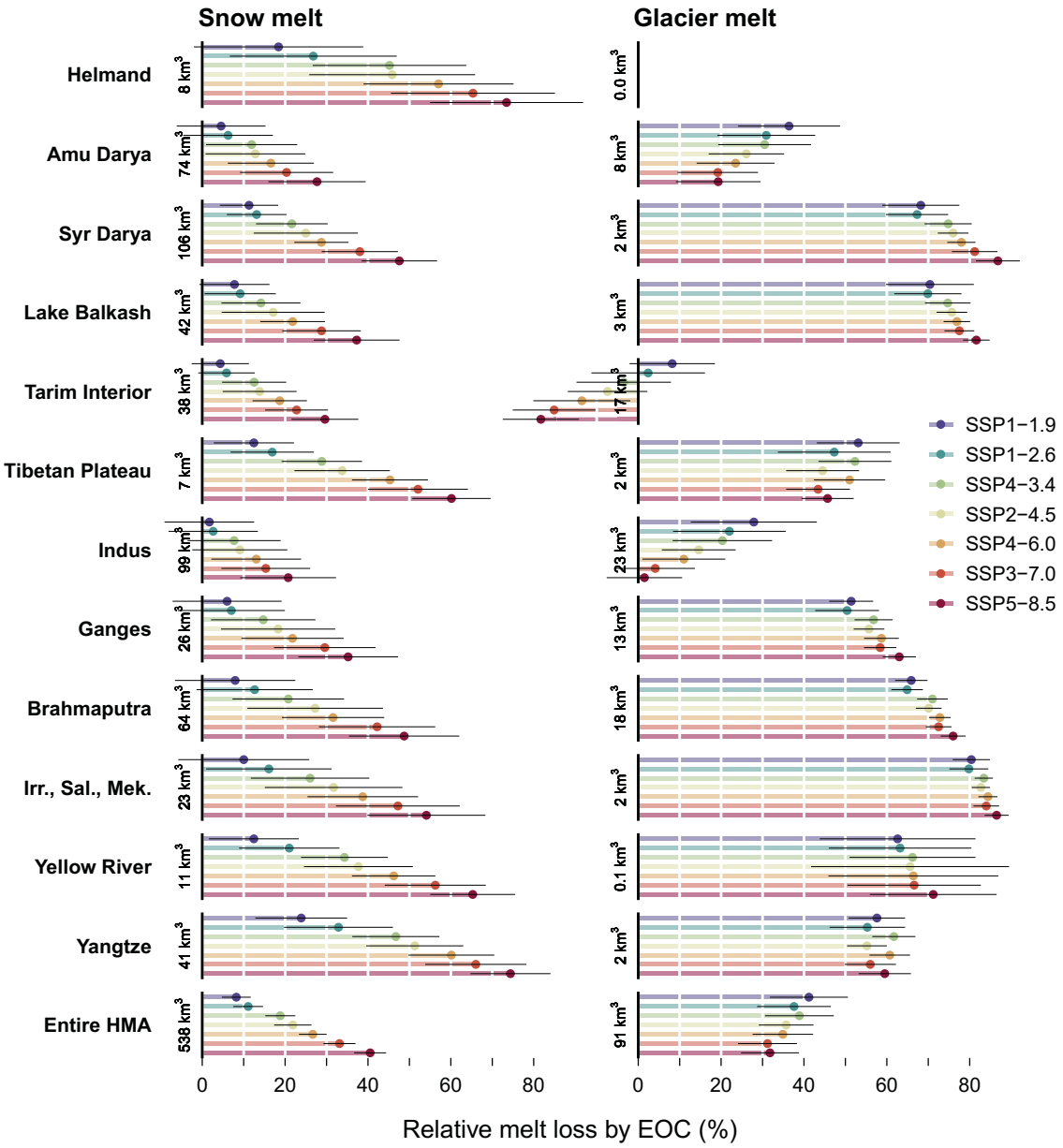

Extended Data Fig. 4 | Projected losses in snow and glacier meltwater by the EOC. Simulated loss of annual snow (left column) and glacier (right column) meltwater by the end of century (2071–2100) for the SSP-RCP ensembles (Supplementary Table 1) with respect to present day (2000–2019) for all basins and the entire HMA (rows). Annual meltwater volume (km^3) in the reference period is annotated in black left of the vertical bars. The errors bars indicate one standard deviation.